

Pressure-Induced Phase Transition and Band Gap Decrease in Semiconducting β - $\text{Cu}_2\text{V}_2\text{O}_7$

Robin Turnbull,* Javier González-Platas, Fernando Rodríguez, Akun Liang, Catalin Popescu, Zhangzhen He, David Santamaría-Pérez, Plácida Rodríguez-Hernández, Alfonso Muñoz, and Daniel Errandonea



Cite This: *Inorg. Chem.* 2022, 61, 3697–3707



Read Online

ACCESS |



Metrics & More

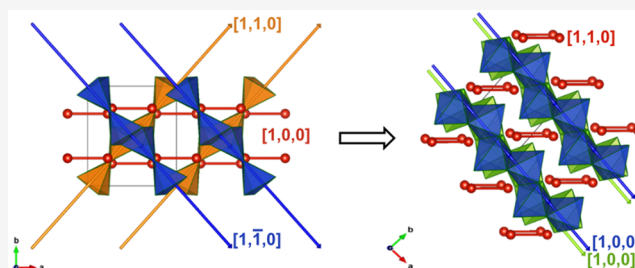


Article Recommendations



Supporting Information

ABSTRACT: The understanding of the interplay between crystal structure and electronic structure in semiconductor materials is of great importance due to their potential technological applications. Pressure is an ideal external control parameter to tune the crystal structures of semiconductor materials in order to investigate their emergent piezo-electrical and optical properties. Accordingly, we investigate here the high-pressure behavior of the semiconducting antiferromagnetic material β - $\text{Cu}_2\text{V}_2\text{O}_7$, finding it undergoes a pressure-induced phase transition to γ - $\text{Cu}_2\text{V}_2\text{O}_7$ below 4000 atm. The pressure-induced structural and electronic evolutions are investigated by single-crystal X-ray diffraction, absorption spectroscopy and *ab initio* density functional theory calculations. β - $\text{Cu}_2\text{V}_2\text{O}_7$ has previously been suggested as a promising photocatalyst for water splitting. Now, these new results suggest that β - $\text{Cu}_2\text{V}_2\text{O}_7$ could also be of interest with regards to barocaloric effects, due to the low phase-transition pressure, in particular because it is a multiferroic material. Moreover, the phase transition involves an electronic band gap decrease of approximately 0.2 eV (from 1.93 to 1.75 eV) and a large structural volume collapse of approximately 7%.



1. INTRODUCTION

1.1. Introduction. Copper vanadate materials constitute an important class of semiconducting inorganic compounds which exhibit a wide variety of chemical compositions: CuV_2O_6 , $\text{Cu}_2\text{V}_2\text{O}_7$, $\text{Cu}_3\text{V}_2\text{O}_8$, $\text{Cu}_4\text{V}_2\text{O}_9$, and $\text{Cu}_5\text{V}_2\text{O}_{10}$. Of these, copper(II) pyrovanadate, $\text{Cu}_2\text{V}_2\text{O}_7$, has been highlighted as a favorable material for the photocatalytic splitting of water into hydrogen and oxygen due to its band gap energy.^{1–3} Therefore, copper vanadate materials may play an essential role in the global shift toward renewable energy sources. $\text{Cu}_2\text{V}_2\text{O}_7$ exhibits three known polymorphs, known as α , β , and γ , all of which are formed at elevated temperatures, either naturally occurring (α and β) or synthesized in the laboratory (γ), and all of which are (meta)stable at ambient conditions.^{4–9}

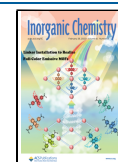
The present work investigates β - $\text{Cu}_2\text{V}_2\text{O}_7$ under high-pressure conditions at ambient temperature to explore the effect of pressure on the crystal and electronic structures. β - $\text{Cu}_2\text{V}_2\text{O}_7$ has a number of interesting and useful properties; for example, β - $\text{Cu}_2\text{V}_2\text{O}_7$ is a semiconducting antiferromagnetic material which has an (indirect) electronic band gap energy of ~ 2 eV, which is optimal for absorbing energy within the solar range.¹⁰ β - $\text{Cu}_2\text{V}_2\text{O}_7$ also exhibits interesting magnetic properties, due to its spin-1/2 honeycomb lattice of Cu^{2+} [$3d^9$] ions, including quasi-1D antiferromagnetism.^{11–13} Finally, β - $\text{Cu}_2\text{V}_2\text{O}_7$ is also known to exhibit a negative thermal expansion

at ambient pressure.^{14,15} None of the $\text{Cu}_2\text{V}_2\text{O}_7$ phases has previously been studied at high pressure; therefore, an additional motivation for this high-pressure investigation is to study mechanical similarities between the negative thermal expansion and pressure-induced volume decrease.

Herein, we report an experimental high-pressure single-crystal synchrotron X-ray diffraction (XRD) study of β - $\text{Cu}_2\text{V}_2\text{O}_7$ under compression up to 4 GPa at ambient temperature. We present unambiguous evidence of a pressure-induced first-order phase transition from the monoclinic β -phase to the triclinic γ -phase between 0.14 and 0.40 GPa. We also investigate the electronic structure via absorption spectroscopy and *ab initio* density functional theory calculations, in particular the optical band gap and sub-band d–d transitions associated with Cu^{2+} coordination complexes, finding the phase transition to be characterized by a 0.2 eV band gap decrease and a decrease in the average crystal field strength. We also report a detailed study of the pressure evolution of both of the crystal structures, associated

Received: December 15, 2021

Published: February 14, 2022



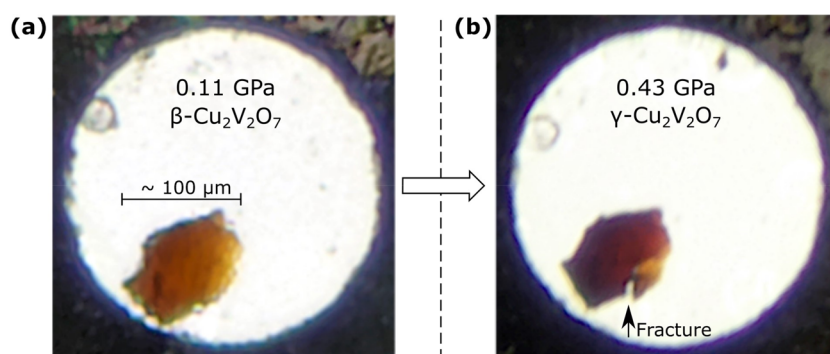


Figure 1. Micrographs of a $\text{Cu}_2\text{V}_2\text{O}_7$ crystal (orange) in the sample chamber of a DAC. (a) $\beta\text{-Cu}_2\text{V}_2\text{O}_7$ crystal at 0.11 GPa. (b) $\gamma\text{-Cu}_2\text{V}_2\text{O}_7$ crystal at 0.43 GPa.

crystallographic parameters and physical properties, including the bulk moduli (via a pressure–volume equation of state (EoS)) and isothermal compressibility tensors of both β - and γ -phases.

2. METHODS

2.1. Sample Preparation. Single crystals of $\beta\text{-Cu}_2\text{V}_2\text{O}_7$ were grown by a flux method using SrV_2O_6 as a flux according to ref 16. A mixture of high-purity CuO , V_2O_5 , and SrCO_3 was ground fully and evenly with ethanol (99%) in an agate mortar. The mixture was packed into a platinum crucible ($40 \times 40 \times 45 \text{ mm}^3$) which was then placed in a homemade electric furnace. The furnace was heated up to $950 \text{ }^\circ\text{C}$ and kept at this peak temperature for 20 h. The furnace was then cooled slowly to $750 \text{ }^\circ\text{C}$ at a rate of $0.5 \text{ }^\circ\text{C/h}$. The furnace was finally cooled down to room temperature at a rate of $100 \text{ }^\circ\text{C/h}$. With the above growth procedure, single crystals of $\beta\text{-Cu}_2\text{V}_2\text{O}_7$ with a size of $3 \times 3 \times 5 \text{ mm}^3$ were obtained by mechanical separation from the crucible. Alternative synthesis methods for $\beta\text{-Cu}_2\text{V}_2\text{O}_7$ also exist.^{2,17}

2.2. Measurements. Angle-dispersive single-crystal XRD data were acquired in two ways. First, data were acquired at ALBA Synchrotron¹⁸ (Barcelona, Spain) on the BL04 - MSPD beamline using a monochromatic beam $\lambda = 0.4246 \text{ \AA}$ focused to a spot size of $20 \times 20 \text{ }\mu\text{m}^2$. A SX165 Rayonix Mar CCD detector was used to record the data. Second, single-crystal XRD data were collected in-house at the University of La Laguna. CrysAlisPro¹⁹ was used to collect, index, scale, and apply numerical absorption corrections to the data. Single-crystal diffraction measurements (SC-XRD) were carried out at room temperature using a Rigaku SuperNOVA diffractometer equipped with an EOS CCD detector and a Mo radiation microsource ($\lambda = 0.71073 \text{ \AA}$). All measurements were processed with the CrysAlis software version 1.171.40.71.²⁰ Numerical absorption correction based on Gaussian integration over a multifaceted crystal model was applied using the ABSORB7 program.²¹ For HP measurements we used a Mini-Bragg DAC from Almax-EasyLab, with an opening angle of 85° and anvil culets of $500 \text{ }\mu\text{m}$ diameter, fitted with a stainless-steel gasket containing a hole of $200 \text{ }\mu\text{m}$ diameter and $75 \text{ }\mu\text{m}$ depth. A 4:1 methanol–ethanol mixture (ME) was used as a pressure-transmitting medium.²² The sample was placed on one of the diamonds anvils (diffracted side) together with a small ruby sphere as a pressure sensor.²³ The structure was refined, for each pressure, using previous results as starting points, on F^2 by full-matrix least-squares refinement using the SHELXL program.²⁴

The optical absorption spectra were acquired using the sample-in sample-out method on the in-house optical setup at the University of Valencia, consisting of a visible–near-IR spectrometer (Ocean Optics Maya2000 Pro), a tungsten filament lamp, fused silica lenses, and reflecting optical objectives. The intensity of the light transmitted through the sample ($I(\omega)$) was normalized against the intensity of the light transmitted through the 16:3:1 methanol–ethanol–water PTM ($I_0(\omega)$). Single crystals of $\beta\text{-Cu}_2\text{V}_2\text{O}_7$, approximately $100 \times 100 \times 40 \text{ }\mu\text{m}^3$ in size, were loaded into membrane-driven DACs with culet sizes of $500 \text{ }\mu\text{m}$. Tungsten gaskets were preindented to $50 \text{ }\mu\text{m}$ thickness,

and then sample chambers $250 \text{ }\mu\text{m}$ in diameter were drilled prior to loading the crystals. Ruby crystals were included in the sample chamber for use as a pressure gauge.

Equations of state (EoS) were fitted to the volume–pressure data using EosFit7-GUI²⁵ whereby the EoS were constrained to second-order ($B_0' = 4$) Birch–Murnaghan equations.²⁶ The validity of the EoS fits was checked via the associated F_E versus f_E plots.²⁷

2.3. Ab Initio Density Functional Theory Calculations. The *ab initio* simulations were carried out within the framework of density functional theory, DFT,²⁸ with the Vienna *ab initio* Simulation Package, VASP.^{29,30} The projector augmented-wave, PAW, and pseudopotentials^{31,32} were employed and the plane-wave kinetic cutoff was extended up to 540 eV to ensure highly converged results. The integrations over the Brillouin zone, BZ, were carried out with k -points special samplings ($4 \times 4 \times 3$ and $5 \times 4 \times 3$ grids, for the low and high-pressure phases, respectively). The exchange–correlation energy was described by means of the generalized gradient approximation, GGA, with the Armiento and Mattsson, AM05, prescription.^{33,34} To treat the strongly correlated states properly, the DFT+U method of Duradev et al.³⁵ was employed. This method utilizes a single parameter, $U_{\text{eff}} = U - J$, where U and J are the effective on-site Coulomb and exchange parameters, respectively. The value used for U_{eff} was 6.5 eV for the Cu atoms.^{36,37} In the present study, the antiferromagnetic configuration was found to be the lower one in energy.

The unit cell parameters and the atomic positions were fully optimized to obtain, at selected volumes, the relaxed structure. The criteria imposed for the optimization were that the forces on the atoms were less than 0.003 eV/\AA , and the deviations of the stress tensors from a diagonal hydrostatic form were lower than 0.1 GPa . In this way, the simulations provide a data set of volumes, energies, and pressures (from the stress tensor) that are fitted with a Birch–Murnaghan equation of state²⁶ to obtain the theoretical equilibrium volume, the Bulk modulus, and the pressure derivatives.

The k -path for the electronic band structure calculations was chosen with the SeeK-path tool.³⁸ The band structure analysis was carried out with the sumo package.³⁹

3. RESULTS AND DISCUSSION

3.1. Visual Observations. The pressure-induced $\beta \rightarrow \gamma$ phase transition is unambiguously confirmed by single-crystal XRD and *ab initio* density functional theory calculations (see the next section). Here, we begin by presenting two visual observations of the $\beta \rightarrow \gamma$ phase transition in the sample. First, the $\sim 2 \text{ eV}$ band gap, which transmits light in the lower energy part of the visible spectrum (red/orange), is sensitive to pressure. In Figure 1 it is clear that the color of the $\text{Cu}_2\text{V}_2\text{O}_7$ crystal becomes darker across the $\beta \rightarrow \gamma$ phase transition, which is associated with a band gap closure of $\sim 0.2 \text{ eV}$ (see “Electronic Structure” section for further details). Second, as indicated by the arrow in Figure 1b, crystal fractures were

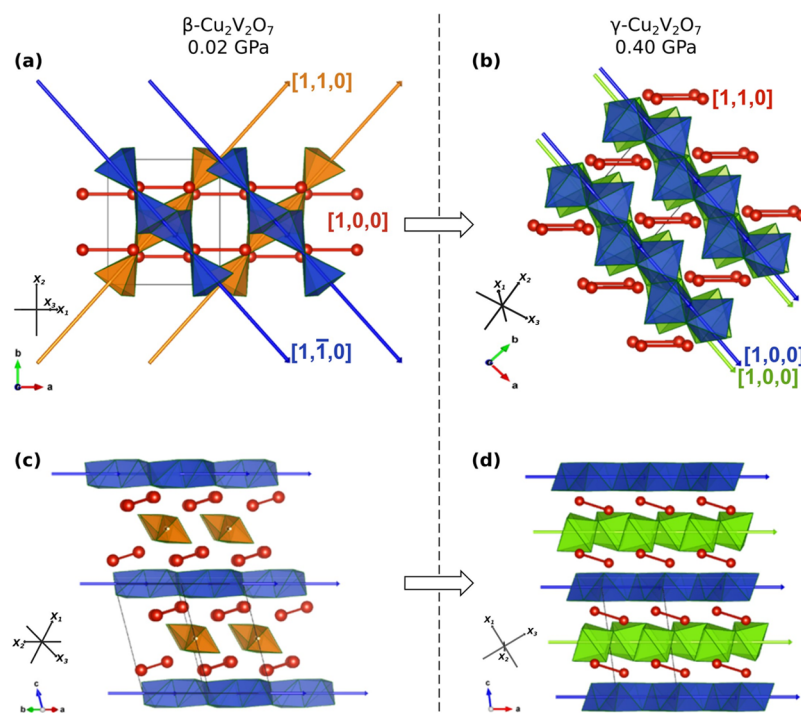


Figure 2. Crystal structures of β - and γ - $\text{Cu}_2\text{V}_2\text{O}_7$. (a) and (b) β - and γ - $\text{Cu}_2\text{V}_2\text{O}_7$ structures, respectively, projected along their c -axes, oriented so that the V–V vectors (red lines) of both structures are mutually parallel on the page. (c) and (d) β - and γ - $\text{Cu}_2\text{V}_2\text{O}_7$ structures, respectively, projected along their ab -planes. Blue (and orange) polyhedra correspond to penta-coordinated CuO_5 units. Green polyhedra correspond to hexa-coordinated CuO_6 units. Red spheres represent vanadium atoms. For the sake of clarity, the VO_4 tetrahedra and the oxygen atoms, which correspond to the vertices of all coordination complexes, are not shown. Blue, orange, and green vectors show the crystallographic direction of the chains. The black axes represent the principal compression axes (discussed in the compressibility section). The crystal structures were rendered in Vesta.⁴⁰ Supplementary crystallographic data for both β - and γ - $\text{Cu}_2\text{V}_2\text{O}_7$ structures can be obtained free of charge from the Cambridge Crystallographic Data Centre (CCDC) under deposition numbers 2123194–2123205.

observed on transition to the γ -phase. Neither crystal fracture nor color change necessarily indicates the existence of a phase transition; however, at such low pressures (<0.5 GPa), the fractures can indicate a large volume collapse associated with a first-order phase transitions. The transition is irreversible on sample decompression.

3.2. Structural Analysis and Phase Transition. The crystal structures of β - and γ - $\text{Cu}_2\text{V}_2\text{O}_7$ are shown in Figure 2, and basic crystallographic information is presented in Table 1. Comprehensive crystallographic information is provided in Tables S1–S3. The crystal structures have previously been

described elsewhere, determined from ambient pressure XRD measurements;⁹ however, for the sake of discussion, the structures of β - and γ - $\text{Cu}_2\text{V}_2\text{O}_7$, as determined in the current work, are briefly described here.

The structure of β - $\text{Cu}_2\text{V}_2\text{O}_7$ is shown in Figures 2a,c. In β - $\text{Cu}_2\text{V}_2\text{O}_7$, all of the Cu^{2+} cations are crystallographically equivalent, and all of them are penta-coordinated by oxygen atoms, thereby forming CuO_5 coordination complexes with a square-based-pyramidal configuration. (For clarity, the CuO_5 units are shown in blue and orange in Figure 2a,c.) All CuO_5 units share edges to form continuous 1D chains which point along the ab -plane diagonals. The chains are also organized into layers, which follow the stacking sequence (ABAB...), where chains in layer A point in the $[1,1,0]$ direction (orange), while chains in layer B point in the $[1,-1,0]$ direction (blue). These A and B layers are interconnected by layers of V_2O_7 dimers, which are each formed by two corner-sharing VO_4 tetrahedra. The V–V vectors, defined by the vanadium atoms in the V_2O_7 units, are all mutually parallel and point along the a -axis (i.e., in the $[1,0,0]$ direction).

The structure of the γ - $\text{Cu}_2\text{V}_2\text{O}_7$ phase is shown in Figure 2b,d. The γ - $\text{Cu}_2\text{V}_2\text{O}_7$ structure has two symmetrically independent Cu^{2+} cations. Half of the Cu^{2+} cations are penta-coordinated in the same way as those in β - $\text{Cu}_2\text{V}_2\text{O}_7$; however, the other half are hexa-coordinated, thereby forming CuO_6 units with octahedral coordination configuration (shown in green in Figure 2b,d). All CuO_5 (CuO_6) units, share edges to form continuous 1D chains, shown in blue (green). All CuO_5 and CuO_6 chains point along the a -axis, or in the $[1,0,0]$ direction. The chains are also organized into layers, which

Table 1. Basic Crystal Data for β - and γ - $\text{Cu}_2\text{V}_2\text{O}_7$ ^a

phase	β - $\text{Cu}_2\text{V}_2\text{O}_7$		γ - $\text{Cu}_2\text{V}_2\text{O}_7$	
	experiment	DFT	experiment	DFT
pressure (GPa)	0.02	0.00	0.40	0.00
crystal system	monoclinic	monoclinic	triclinic	triclinic
space group	$C2/c$	$C2/c$	$\bar{P}1$	$\bar{P}1$
a (Å)	7.6858(11)	7.7660	5.080(5)	5.0540
b (Å)	8.0341(9)	7.9205	5.8098(16)	5.8041
c (Å)	10.121(3)	10.0631	9.380(4)	9.4689
α (deg)	90	90	100.00(3)	99.80
β (deg)	110.39(2)	109.36	97.20(6)	97.88
γ (deg)	90	90	97.18(5)	97.15
V (Å ³)	585.8(2)	584.0	267.4(3)	268.0
Z	4	4	2	2

^aComprehensive experimental crystallographic information is provided in Tables S1–S3.

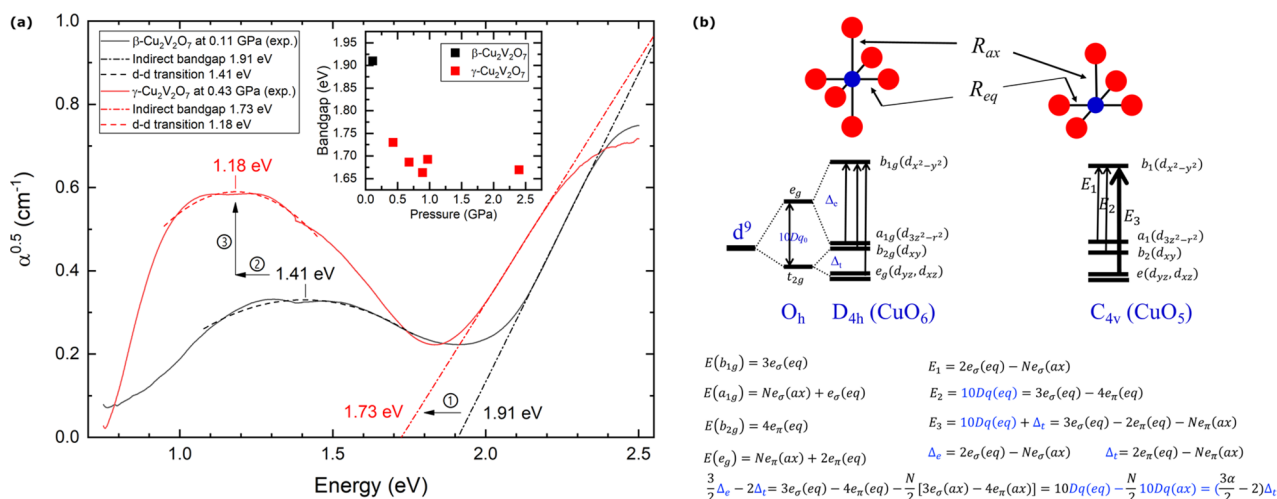


Figure 3. Absorption spectra and schematic energy level diagrams. (a) Experimental absorption spectra. Black lines correspond to β -Cu₂V₂O₇ at 0.11 GPa. Red lines correspond to γ -Cu₂V₂O₇ at 0.43 GPa. Dashed and dotted lines correspond to the linear fits determining the band gap energy. The band gap energies of β - and γ -Cu₂V₂O₇ were experimentally determined to be 1.91 and 1.73 eV respectively. Dashed lines correspond to Gaussian fits determining the d-d transition energy. Inset: the experimental band gap as a function of pressure. The individual fitted spectra are shown in Figure S2. (b) Schematic energy level diagrams of the elongated octahedral CuO₆ (nearly D_{4h}) and elongated pyramidal CuO₅ (nearly C_{4v}) complexes.

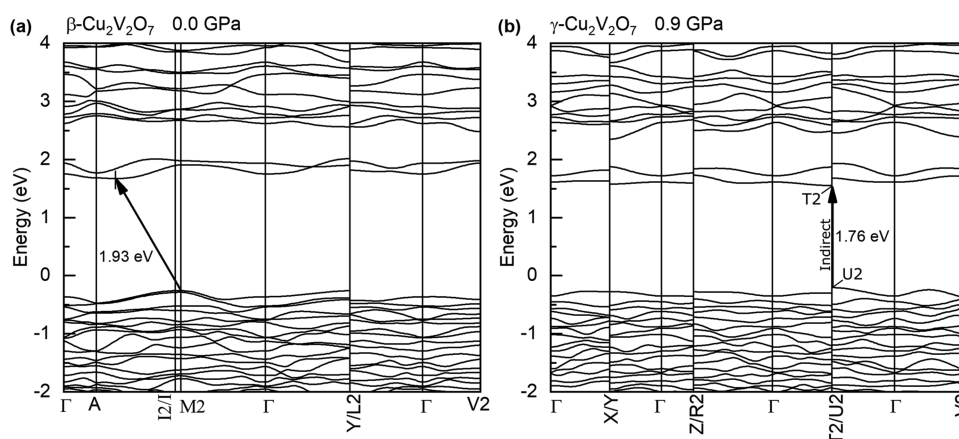


Figure 4. Calculated electronic band structures of β - and γ -Cu₂V₂O₇. (a) β -Cu₂V₂O₇ at 0.0 GPa. (b) γ -Cu₂V₂O₇ at 0.9 GPa.

follow the stacking sequence (ABAB...), where chains in layer A contain only CuO₅ units (blue), while chains in layer B contain only CuO₆ units (green). These A and B layers are again interconnected by layers of V₂O₇ dimers. The V–V vectors are all mutually parallel and point along the *ab*-plane diagonal (i.e., in the [1,1,0] direction).

It is clear from Figure 2 that the crystal structures of β - and γ -Cu₂V₂O₇ are closely related. Both structures are characterized by alternating layers of chains of CuO_x units, whereby the layers are interconnected by mutually parallel V₂O₇ units. The orientation of the V–V vectors (red) relative to the CuO₅ chains (blue) is the same in both structures (shown in Figure 1). Therefore, the $\beta \rightarrow \gamma$ phase transition can be qualitatively described by two factors: (1) an increase of coordination number, from 5 to 6, of all CuO₅ units in alternating layers and (2) a transformation of those layers (approximately by a reflection in the *ac*-plane) so that all CuO₆ chains become parallel to the CuO₅ chains.

Cu₂V₂O₇ has not been studied previously under high-pressure conditions; therefore, this is the first time that the $\beta \rightarrow \gamma$ phase transition has been observed to be induced by

pressure. Bearing in mind that β -Cu₂V₂O₇ has been found to occur naturally in fumarolic areas and that the low pressure required to induce the $\beta \rightarrow \gamma$ phase transition (<0.4 GPa) occurs naturally in the earth's crust, the present work shows that γ -Cu₂V₂O₇ may also occur naturally although it has not yet been discovered. The $\beta \rightarrow \gamma$ phase transition has previously been observed to be induced by high temperatures (~700 °C) at ambient pressures.^{7,8} Therefore, the $\beta \rightarrow \gamma$ phase boundary must have a steep negative slope in pressure–temperature space because it can be crossed by increasing either temperature (~700 °C) or pressure (<0.4 GPa) from ambient conditions. *Ab initio* density functional theory (DFT) calculations of enthalpy, for the beta and gamma phases, found that the triclinic phase becomes the more stable phase at 0.1 GPa and 0 K (see Figure S1).

3.3. Electronic Structure. The optical properties, and thus the piezo- and thermochromic properties, exhibited by β - and γ -Cu₂V₂O₇ can be explained by the optical transmission window defined by the interband charge transfer transitions (optical band gaps) and the sub-band absorption of Cu²⁺ d-levels (see Figure 3). The relative variations in transition

energies and oscillator strength (absorption coefficient) with temperature and/or pressure determine these properties. Therefore, understanding these properties requires a precise knowledge of how structural variations (determined via XRD) affect the electronic structure.

The electronic structures of β - and γ -Cu₂V₂O₇ were investigated via absorption spectroscopy measurements and *ab initio* simulations. There are two regions of interest in the adsorption spectra in Figure 3: first, on the right-hand side (above 1.8 eV), the optical band gap edges; second, on the left-hand side (below 1.8 eV), the absorption associated with d–d electronic transitions of Cu²⁺.

3.3.1. Band Structure. We first discuss the optical band gap energies. The band gap energies of β - and γ -Cu₂V₂O₇ were experimentally determined to be 1.91 and 1.73 eV, respectively, thereby corresponding to a band gap collapse of 0.18 eV (~9%) across the $\beta \rightarrow \gamma$ phase transition (as shown by arrow 1 in Figure 3). The β -phase band gap energy of 1.91 eV is in good agreement with the previously reported experimental values of 1.78 eV (ref 37), 1.91 eV (ref 3), and 2.21 eV (ref 41) and the theoretically calculated value of 2.00 eV.¹⁰ The band gap of γ -Cu₂V₂O₇ has not previously been reported. Density functional calculations were also carried out to obtain the full electronic band structures, as indicated in Figure 4, revealing both band gaps to be indirect. The calculated (experimental) band gap energies of β - and γ -Cu₂V₂O₇ are 1.93 eV (1.91 eV) and 1.76 eV (1.73 eV) respectively, thereby showing excellent agreement between experiment and theory. The pressure evolution of the calculated band gaps up to 10 GPa is shown in Figure S3. The experimental band gaps as a function of pressure up to 2.4 GPa are shown in the inset in Figure 3. Additionally, the DOS (total density of states) and the projected density of states (Figure S4) are very similar for both phases. The upper level of the valence band is contributed to mainly by Cu-3d and O-2p states, while the O 2s states are located in the lower part of the valence band. As for the conduction band, the major contribution comes from the V 3d states.

3.3.2. Sub-Band Absorption. We now discuss the sub-band absorption (below 1.8 eV) associated with d–d electronic transitions of Cu²⁺. The broad Gaussian-shaped absorbing regions observed in the sub-band gap energy region below 1.8 eV (see Figure 3) are due to d–d electronic transitions of Cu²⁺ and the transition energies can be thoroughly explained by crystal-field (CFM) and angular overlap (AOM) models.^{42,43} The maxima, bandwidth, and oscillator strength of these bands strongly depend on the Cu²⁺ local symmetry of the CuO₅ or CuO₆ coordination complexes.⁴⁴ Figure 3b shows schematic energy level diagrams of the elongated octahedral CuO₆ (nearly *D*_{4h}) and elongated pyramidal CuO₅ (nearly *C*_{4v}) complexes, and the corresponding energies as a function of the σ and π bonding AOM parameters e_σ and e_π for the equatorial (eq) and axial (ax) ligands.⁴² The crystal-field strength scales with the bond distance in oxides as a power of 5: $10Dq(R) = C/(R^5)$, where R is the bond length. This R -dependence is found from basic CF theory,^{43,45,46} and it has also been observed experimentally in several high-pressure experiments in transition metal oxides and fluorides involving Cr³⁺ (ref 47), Fe³⁺ (refs 48–50), or Co²⁺ (ref 51) within an experimental accuracy of 5.0 ± 0.5 . Therefore, the ratio of the transition energies in the β - and γ -phases is given by

$$\frac{E(e \rightarrow b_1)\gamma}{E(e \rightarrow b_1)\beta} = \left(\frac{R_{\text{eq}}^\beta}{R_{\text{eq}}^\gamma} \right)^5 \quad (1)$$

The derivation of eq 1 is provided in the Supporting Information. Taking the average $R_{\text{eq}}^\beta = 1.95$ Å and $R_{\text{eq}}^\gamma = 2.01$ Å from the experimental XRD data, the reduction in $E(e \rightarrow b_1)$ along the $\beta \rightarrow \gamma$ phase transition should be 0.86 according to the model. The experimental energy ratio between 1.41 eV (β) and 1.18 eV (γ) gives a ratio of 0.84 in excellent agreement with the model.

It must be noted that although R_{eq}^β and R_{eq}^γ are derived as an average of the four short Cu–O distances obtained from XRD for CuO₅ the standard deviation of such distances is below $\sigma = 0.012$ Å in the β -phase and 0.07 Å in the γ -phase. In fact, the slight double-humped band observed in both phases (Figure 3a) may be due to low-symmetry local distortion of CuO₅ beyond *C*_{4v}. This symmetry lowering would additionally split the doubly degenerate e levels into two singlets (xz , yz) yielding additional broadened bands.

In Figure 3, both sub-band absorption spectra are completely determined by the CuO₅ polyhedra because d–d transitions are, in the first approximation, parity-forbidden in centrosymmetric compounds like CuO₆ (Laporte rule), although they can occur via electron–phonon coupling, thereby contributing only weakly to the observed spectrum. An additional simplification is that the $e(d_{xz}, d_{yz}) \rightarrow b_1(d_{x^2-y^2})$ electric-dipole transition, which is allowed in CuO₅, has an oscillator strength which is an order of magnitude higher than any of the other d–d transitions in CuO₅ (involving the $b_2(d_{xy})$ and $a_1(d_{3z^2-r^2})$ levels), or in the nearly *D*_{4h} elongated CuO₆ ($e_g, b_{2g}, a_{1g} \rightarrow b_1$).^{45,52} Therefore, only one transition is needed to explain the sub-band absorption peaks.

The sub-band absorption maxima are found at 1.41 and 1.18 eV for β - and γ -Cu₂V₂O₇, respectively, thereby corresponding to a decrease in the transition energy of approximately 0.23 eV across the phase transition (as indicated by arrow 2 in Figure 3). The transition energy (or d-level splitting) in CuO₅ is determined by the strength of the crystal field, which is in turn determined by the Cu–O bond lengths. The decrease in transition energy across the phase transition implies a decrease in crystal field strength and therefore an increase in Cu–O bond length. This is consistent with the Cu–O bond lengths determined from our XRD data (see Figure S5). For example, the average CuO₅ equatorial (axial) Cu–O distance increases from 1.95 (2.25) Å to 2.01 (2.33) Å across the phase transition. For comparison, these values are in agreement with those found in α -CuMoO₄, wherein the $e \rightarrow b_1$ absorption energy is identified as 1.49 eV in CuO₅ units which have an average equatorial Cu–O distance of 1.93 Å (ref 52). A similar energy of 1.7 eV was also reported in YBa₂Cu₃O_y in ref 53.

The observed oscillator strength (absorption coefficient) largely depends on the orientation of the transition dipole, which in this case is in the basal plane of the CuO₅ polyhedra, and the electric field vector of the incident light used in the experiment. Because the γ -phase has exactly half the number of CuO₅ polyhedra of the β -phase, a drop in oscillator strength would be expected across the phase transition, however the opposite is observed (as shown by arrow 3 in Figure 3). This can be attributed to the spatial orientation of the single crystal sample relative to the incident light. It is not possible to comment on the crystallographic orientation in the absorption

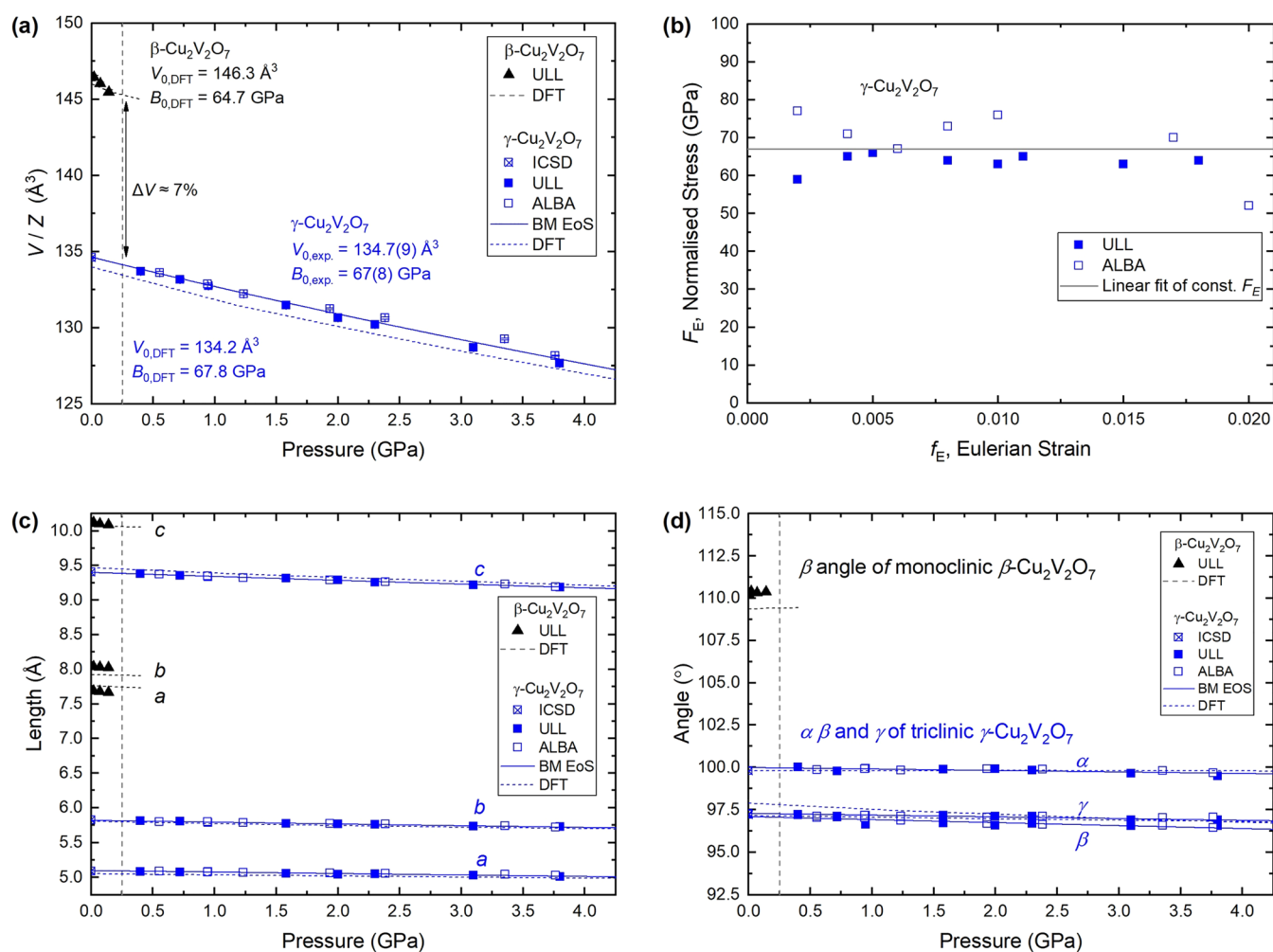


Figure 5. Equation of state and pressure-response of crystal lattice parameters in β - and γ - $\text{Cu}_2\text{V}_2\text{O}_7$ to 4 GPa. (a) Normalized unit cell volume as a function of increasing pressure up to 4 GPa. (b) Normalized stress as a function of Eulerian strain for the experimental data. (c) Lattice constants a , b , and c , and (d) unit cell angles, α , β , and γ , as functions of pressure. Data corresponding to β - $\text{Cu}_2\text{V}_2\text{O}_7$ (γ - $\text{Cu}_2\text{V}_2\text{O}_7$) are shown in black (blue). (a, c, d) Solid (dashed) lines correspond to second-order Birch–Murnaghan equations of state (BM EoS) fitted to the experimental (calculated) data. Vertical dashed gray lines show the approximate phase transition pressure. The labels “ULL” and “ALBA” respectively signify data collected in-house at the University of La Laguna and at ALBA Synchrotron. ICSD refers to the ambient condition (atmospheric pressure and room temperature) γ - $\text{Cu}_2\text{V}_2\text{O}_7$ structure of ref 9 taken from the Inorganic Crystal Structure Database.

spectra because the XRD measurements were carried out independently on different single crystal samples.

3.4. Bulk Modulus. The $\beta \rightarrow \gamma$ phase transition is unambiguously categorized as first-order according to the plot of the normalized unit cell volume (V/Z) as a function of pressure, as shown in Figure 5a. A volume collapse of approximately 7% is observed across the phase transition in both experimental and calculated data. The normalized ambient pressure volumes, V_0 , and bulk moduli, B_0 , were determined by fitting Birch–Murnaghan (BM) equations of state (EoS) truncated to second-order in energy ($B_0' = 4$) to the data. Due to the low phase transition pressure, only four experimental data points were obtained for β - $\text{Cu}_2\text{V}_2\text{O}_7$. Therefore, the theoretical data (black dashed line in Figure 5a) are used for the discussion. The excellent reliability of the calculated data is clearly shown in Figure 5 (dashed lines) by the close agreement with the experimentally determined lattice parameters.

The normalized volume at ambient pressure, V_0 , and bulk modulus, B_0 , for both β - and γ - $\text{Cu}_2\text{V}_2\text{O}_7$ (summarized in Figure 5a) are as follows: For the low-pressure phase, β -

$\text{Cu}_2\text{V}_2\text{O}_7$, the DFT data are fitted with $V_{0,\text{DFT}} = 146.3 \text{ \AA}^3$ and $B_{0,\text{DFT}} = 64.7 \text{ GPa}$. For the high-pressure phase, γ - $\text{Cu}_2\text{V}_2\text{O}_7$, the parameters are $V_{0,\text{DFT}} = 134.2(9) \text{ \AA}^3$ and $B_{0,\text{DFT}} = 67.8 \text{ GPa}$, which are in excellent agreement with those determined from the experimental data: $V_{0,\text{exp}} = 134.7(9) \text{ \AA}^3$ and $B_{0,\text{exp}} = 67(8) \text{ GPa}$. Numbers in parentheses are the estimated standard error in the least significant digit. These bulk moduli are comparable to some of the lowest observed in other vanadate materials, for example $\text{Cu}_3\text{V}_2\text{O}_8$ and $\text{Zn}_2\text{V}_2\text{O}_7$, at 52(2) and 58(9) GPa, respectively.^{54,55}

Figure 5b shows the normalized stress, F_E , as a function of Eulerian strain, f_E . The F_E versus f_E plot provides assessment of the quality of the fitted EoS, whereby a zero-gradient fit to the data indicates that a second-order truncation of the BM EoS is suitable (see ref 27 for more details), as is the case for γ - $\text{Cu}_2\text{V}_2\text{O}_7$ (see Figure 5b).

3.5. Isothermal Compressibility. The isothermal compressibility tensor describes the principal axes of compression which, for any crystal system, constitute a unique set of orthogonal axes along which compressibility is described by a linear function of pressure.⁵⁷ The magnitudes (compressibil-

ities, K) and directions of the principal axes of compression (X_1 , X_2 , and X_3) for β - and γ - $\text{Cu}_2\text{V}_2\text{O}_7$ are presented in Table 2.

Table 2. Compressibility Data for β - and γ - $\text{Cu}_2\text{V}_2\text{O}_7$ ^a

β - $\text{Cu}_2\text{V}_2\text{O}_7$			
axis	compressibility, K (GPa^{-1})	direction $[u, v, w]$	approx. direction $[x, y, z]$
X_1	31.8×10^{-3}	0.8031, 0.0000, 0.5959	4, 0, 3
X_2	5.2×10^{-3}	0.0000, 1.0000, 0.0000	0, 1, 0
X_3	32.1×10^{-3}	0.7818, 0.0000, -0.6236	4, 0, -3
γ - $\text{Cu}_2\text{V}_2\text{O}_7$			
axis	compressibility, K (GPa^{-1})	direction $[u, v, w]$	approx. direction $[x, y, z]$
X_1	5.75×10^{-3}	-0.6089, 0.3500, 0.7118	-12, 7, 14
X_2	4.59×10^{-3}	-0.0136, 0.9924, -0.1222	0, 1, 0
X_3	2.28×10^{-3}	0.9262, 0.2496, 0.2826	4, 1, 1

^aThe principal compression axes (X_1 , X_2 , and X_3) are represented by black arrows in Figures 2 and 6. The data in the table were calculated using the lattice parameters from the single crystal XRD analysis (Tables S1–S3) and the PASCAL principal axis strain calculator.⁵⁶

The principal axes of compression of β - $\text{Cu}_2\text{V}_2\text{O}_7$ reveal a pronounced anisotropic compressibility (see Figures 2 and 6) which is herein rationalized in terms of the underlying crystal structure. The principal axis of minimal compression, in this case X_2 , points in the $[0,1,0]$ direction and has a compressibility of $5.2 \times 10^{-3} \text{ GPa}^{-1}$. Therefore, the least

compressible direction in β - $\text{Cu}_2\text{V}_2\text{O}_7$ exactly corresponds to the crystallographic b -axis and points exactly between the layers of chains of edge-sharing CuO_5 units (which lie in the ab -plane). Additionally, X_2 dissects the smallest angle between the two different types of chains (see Figure 2a) thereby pinpointing the direction of maximum strength.

In contrast, the intermediate and major principal compression axes (X_1 and X_3) in β - $\text{Cu}_2\text{V}_2\text{O}_7$ are approximately 6 times more compressible than X_2 , with mutually comparable compressibilities of 31.8×10^{-3} and $32.1 \times 10^{-3} \text{ GPa}^{-1}$ respectively. Both X_1 and X_3 lie in ac -plane, and as per the definition of the principal axes of compression, they are related by a rotation of 90° since their directions are $[4,0,3]$ and $[4,0,-3]$, respectively. It is important that both of X_1 and X_3 lie in the ac -plane because they share this description with all of the CuO_5 lone electron pairs (LEPs) (see Figure 6a,c). Specifically, each penta-coordinated CuO_5 units possesses an axial LEP, opposite the axial oxygen atom, which points toward the location where a sixth oxygen would make a complete octahedron. The directions of the LEPs are indicated by blue arrows in Figure 6. The LEPs are exactly perpendicular to the principal axis of minimal compression, X_2 (equivalently, the b -axis); therefore, it is clear that the LEPs are responsible for the highly anisotropic compressibility of β - $\text{Cu}_2\text{V}_2\text{O}_7$. A similar phenomenon has also been observed in iodates.⁵⁸

The principal axes of compression of γ - $\text{Cu}_2\text{V}_2\text{O}_7$ reveal a much less pronounced anisotropic compressibility in contrast to that of β - $\text{Cu}_2\text{V}_2\text{O}_7$. Where the principal axes of major and minor compression in the β -phase respectively had compressi-

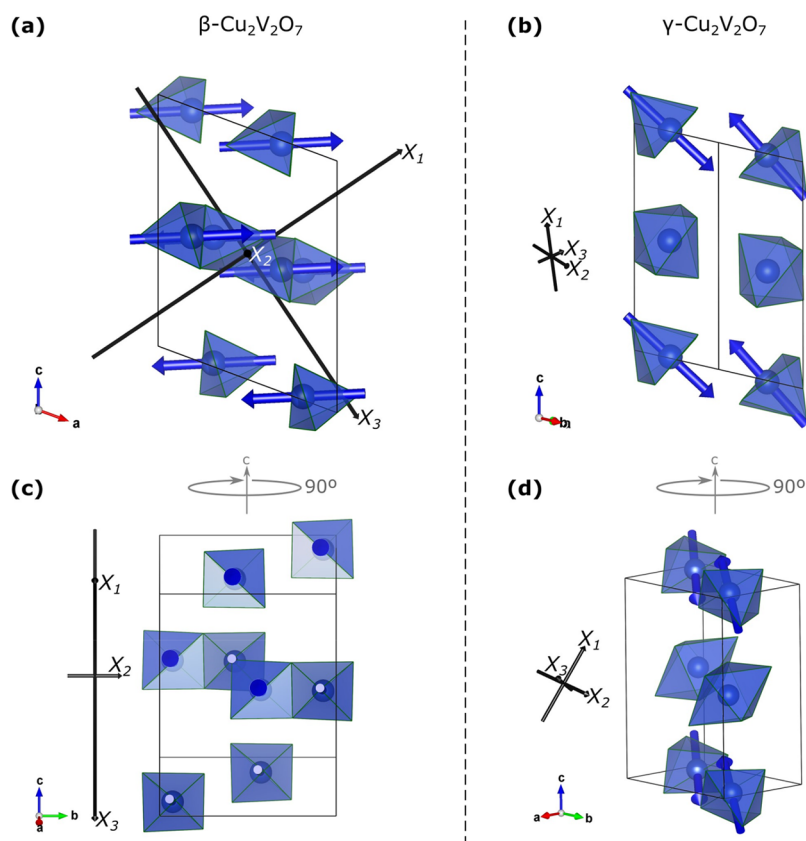


Figure 6. Crystal structures of β - and γ - $\text{Cu}_2\text{V}_2\text{O}_7$ showing the lone electron pair (LEP) vectors. (a, c) β - $\text{Cu}_2\text{V}_2\text{O}_7$ and (b, d) γ - $\text{Cu}_2\text{V}_2\text{O}_7$. Blue arrows show the direction of the LEP on each CuO_5 unit (blue polyhedra). Black arrows represent the compressibility axes. The arrow length shown in the figure is proportional to the magnitude of compressibility for the corresponding axis.

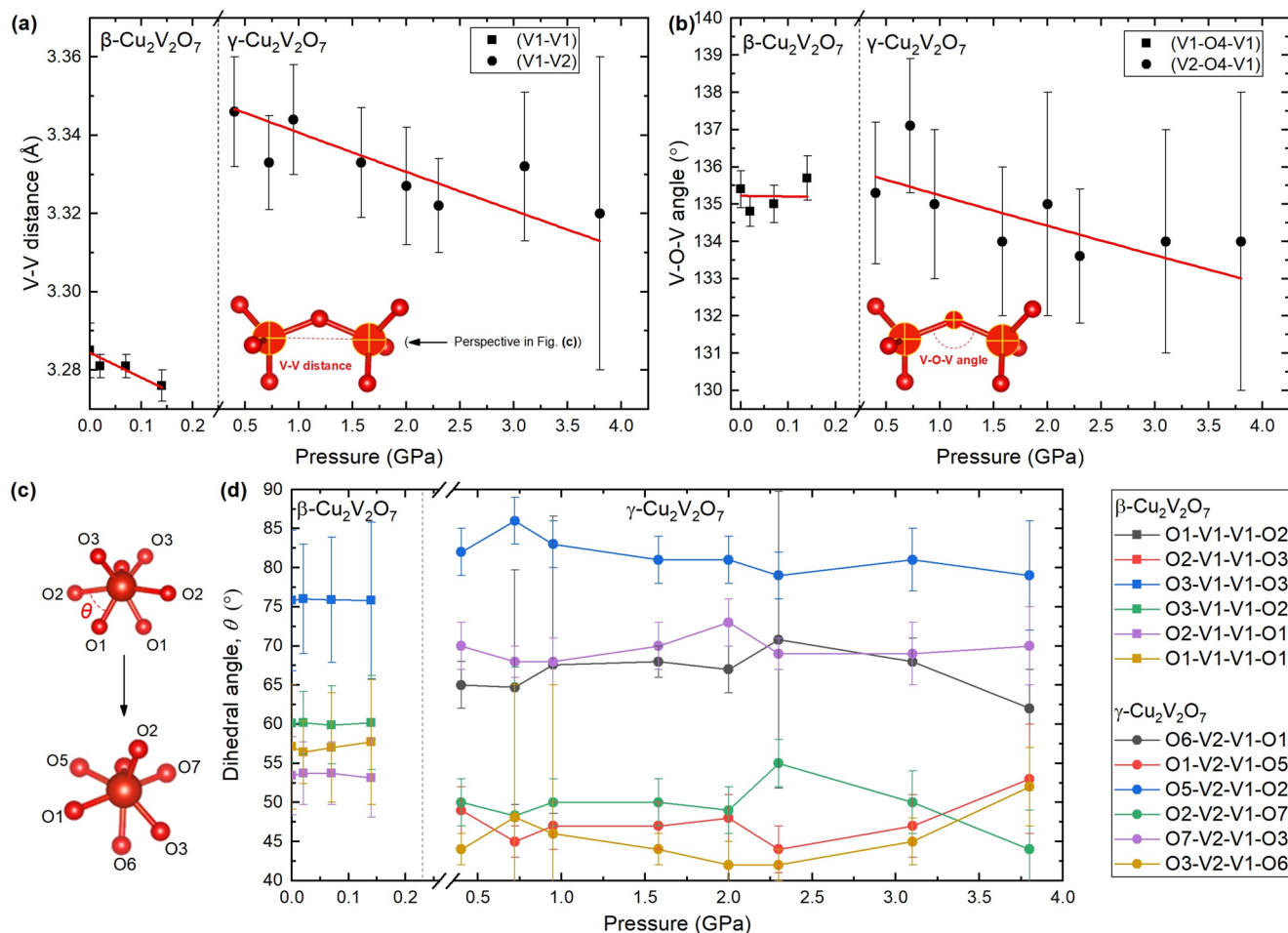


Figure 7. Pressure evolution of the V_2O_7 dimers in β - and γ - $\text{Cu}_2\text{V}_2\text{O}_7$. (a) Interatomic distance between vanadium atoms. (b) Angle between the V–O bonds, forming the V–O–V angle. (c) V_2O_7 molecules viewed along the axis defined by the vanadium atoms before (top) and after (bottom) the phase transition. (d) Pressure evolution of the O–V–(O)–V–O dihedral angles, θ .

bilities of 32.1×10^{-3} and $5.2 \times 10^{-3} \text{ GPa}^{-1}$ (a difference of a factor of approximately 6), in the γ -phase, they have compressibilities of 5.75×10^{-3} and $2.28 \times 10^{-3} \text{ GPa}^{-1}$ (a difference of a factor of approximately 2). Interestingly, the most compressible axis in the γ -phase is roughly equivalent to the least compressible axis in the β -phase in terms of compressibility.

3.6. Pressure-Induced Structural Evolution/Relation to Nonlinear Thermal Expansion. The β - $\text{Cu}_2\text{V}_2\text{O}_7$ structure exhibits negative thermal expansion (NTE) at ambient pressures. The primary mechanism for the NTE is believed to relate primarily to a transverse vibrational mode associated with the oxygen atom which bridges the VO_4 tetrahedra in the V_2O_7 chains ($\text{O}_3\text{V}-\text{O}-\text{VO}_3$). The V_2O_7 units interlink the chains of edge-sharing CuO_x units; therefore, a vibrational mode perpendicular to the V–O–V bridge causes a reduction in the time-averaged distance between the vanadium atoms, thereby pulling the layers closer together and reducing the unit volume.^{14,15}

Since the layers lie in the ab -plane, a reduction in the lattice constant c corresponds to a decrease in the interlayer distance. As shown in Figure 5c, all lattice constants for both phases decrease monotonically with increasing pressure. In the present work, the interlayer spacing abruptly decreases from 4.7429 to 4.5294 Å across the $\beta \rightarrow \gamma$ phase transition, thereby corresponding to a change in interlayer spacing of -0.2135

Å. Because only the time-averaged atomic positions can be observed in XRD measurements, the vibrational modes cannot be observed directly. However, the time-averaged V_2O_7 unit provides insight regarding the pressure-induced structural behavior. For example, Figure 7a shows the intervanadium (V–V) distance as a function of pressure. The V–V distance decreases with pressure in both phases; however, it jumps by +0.1 Å across the $\beta \rightarrow \gamma$ phase transition. The normalized unit cell volume decreases across the transition, therefore the V–V distance is clearly not the dominating factor in the volume decrease. Additionally, as shown in Figure 7b, the V–O–V angle, formed by the bridging oxygen atom, appears to remain constant in the β -phase, whereas it decreases with pressure in the γ -phase and exhibits no clear jump across the phase transition. Therefore, the V–O–V angle is also not responsible for the large volume collapse. The Cu–O bond distances also remain roughly constant over the full pressure range (see Figure S5), and in fact, the volume of the CuO_x coordination complexes appears to increase (see Figure S6). The key to the volume collapse of $\Delta V \approx 7\%$ therefore likely lies with the mutual rotation of the VO_4 units. According to the XRD data, when viewed along the V–V direction (as shown in Figure 7c) the $\text{O}_3\text{V}-\text{O}-\text{VO}_3$ configuration goes from staggered in the β -phase to slightly eclipsed in the γ -phase. In a perfectly staggered configuration all of the O–V–(O)–V–O dihedral angles, θ , would be equal to 60° . All V_2O_7 dihedral angles are

plotted as a function of pressure in Figure 7d, whereby it is clear that the dihedral angles in the γ -phase exhibit a larger deviation from 60° than those in the β -phase. This is important because it suggests that the relative rotation of the VO_4 units (which comprise the V_2O_7 dimers) is an important characteristic of the volume collapse. This supports previous ambient pressure investigations which suggest that mutual rotation of the VO_4 molecular units, suggested by vibrational spectroscopy measurements, underpin the negative thermal expansion mechanism.^{14,15}

4. CONCLUSIONS

We report an experimental high-pressure single-crystal synchrotron XRD study of $\text{Cu}_2\text{V}_2\text{O}_7$ under compression to 4 GPa at ambient temperature. The results unambiguously reveal a previously unknown first-order pressure-induced phase transition from monoclinic β - $\text{Cu}_2\text{V}_2\text{O}_7$ to triclinic γ - $\text{Cu}_2\text{V}_2\text{O}_7$ below 0.40 GPa. The $\beta \rightarrow \gamma$ phase transition is associated with a volume collapse of approximately 7%, an increase in oxygen coordination (from 5 \rightarrow 6) of half of the Cu^{2+} coordination complexes, and a reorientation of 1-dimensional chains composed of edge sharing CuO_6 units. The phase transition is also characterized by an indirect \rightarrow indirect electronic band gap decrease of approximately 0.2 eV as measured by absorption spectroscopy (1.93 \rightarrow 1.75 eV) and calculated via density functional calculations (1.93 \rightarrow 1.76 eV). The band gap of γ - $\text{Cu}_2\text{V}_2\text{O}_7$ has been measured here for the first time, indicating that γ - $\text{Cu}_2\text{V}_2\text{O}_7$ has better potential as a photocatalyst for water splitting than does β - $\text{Cu}_2\text{V}_2\text{O}_7$ due to its lower band gap and therefore greater absorption of visible light. The pressure evolution of the crystal lattice parameters and isothermal compressibility tensor are also reported here for the first time. The compressibility of β - $\text{Cu}_2\text{V}_2\text{O}_7$ is found to be highly anisotropic, with the axis of minimal compression being approximately six times less compressible than the other two axes. The anisotropic compressibility is rationalized in terms of the underlying crystal structures and the presence and spatial orientation of lone-electron pairs on the constituent CuO_5 units. Due to the low transition pressure at ambient temperature, large volume collapse, and the fact that $\text{Cu}_2\text{V}_2\text{O}_7$ is a multiferroic material, this combined experimental and theoretical investigation into the high-pressure structural and electronic evolution of $\text{Cu}_2\text{V}_2\text{O}_7$ suggests that in addition to the previously suggested uses in photocatalytic water splitting $\text{Cu}_2\text{V}_2\text{O}_7$ could also be a very relevant material for exploring solid state barocaloric effects, such as solid-state refrigeration technologies based on crystals which are environmentally friendly. For a material to be promising in terms of barocaloric effects it needs to exhibit, among other qualities, a first-order like phase transition involving large structural changes (e.g., volume change) near room temperature induced by small pressure drifts (i.e., of the order of 0.1 GPa). As shown in the current work, $\text{Cu}_2\text{V}_2\text{O}_7$ appears to meet these specifications.

■ ASSOCIATED CONTENT

SI Supporting Information

The Supporting Information is available free of charge at <https://pubs.acs.org/doi/10.1021/acs.inorgchem.1c03878>.

Detailed crystallographic tables; calculated relative enthalpy; absorption spectra; calculated band gap energies; density of states and projected density of

states; derivation of the ratio of sub-band transition energies; pressure evolution of the Cu–O bonds in CuO_5 and CuO_6 polyhedra; and CuO_x and VO_4 polyhedral volumes as functions of pressure (PDF)

Accession Codes

CCDC 2123194–2123205 contain the supplementary crystallographic data for this paper. These data can be obtained free of charge via www.ccdc.cam.ac.uk/data_request/cif, or by emailing data_request@ccdc.cam.ac.uk, or by contacting The Cambridge Crystallographic Data Centre, 12 Union Road, Cambridge CB2 1EZ, UK; fax: +44 1223 336033.

■ AUTHOR INFORMATION

Corresponding Author

Robin Turnbull – *Departamento de Física Aplicada - Instituto de Ciencia de Materiales, MALTA Consolider Team, Universidad de Valencia, Edificio de Investigación, 46100 Valencia, Spain; orcid.org/0000-0001-7912-0248; Email: robin.turnbull@uv.es*

Authors

Javier González-Platas – *Departamento de Física - Instituto Universitario de Estudios Avanzados en Física Atómica, Molecular y Fotónica (IUDEA), MALTA Consolider Team, Universidad de La Laguna, Tenerife E-38204, Spain; orcid.org/0000-0003-3339-2998*

Fernando Rodríguez – *MALTA Consolider Team, Departamento de Ciencias de la Tierra y Física de la Materia Condensada, Facultad de Ciencias, Universidad de Cantabria, 39005 Santander, Spain; orcid.org/0000-0002-7237-7443*

Akun Liang – *Departamento de Física Aplicada - Instituto de Ciencia de Materiales, MALTA Consolider Team, Universidad de Valencia, Edificio de Investigación, 46100 Valencia, Spain; orcid.org/0000-0002-0515-0484*

Catalin Popescu – *CELLS-ALBA Synchrotron Light Facility, 08290 Cerdanyola del Valles, Barcelona, Spain*

Zhangzhen He – *State Key Laboratory of Structural Chemistry, Fujian Institute of Research on the Structure of Matter, Chinese Academy of Sciences, Fuzhou, Fujian 350002, China*

David Santamaría-Pérez – *Departamento de Física Aplicada - Instituto de Ciencia de Materiales, MALTA Consolider Team, Universidad de Valencia, Edificio de Investigación, 46100 Valencia, Spain*

Plácida Rodríguez-Hernández – *Departamento de Física, Instituto de Materiales y Nanotecnología, MALTA Consolider Team, Universidad de La Laguna, La Laguna E-38204 Tenerife, Spain; orcid.org/0000-0002-4148-6516*

Alfonso Muñoz – *Departamento de Física, Instituto de Materiales y Nanotecnología, MALTA Consolider Team, Universidad de La Laguna, La Laguna E-38204 Tenerife, Spain; orcid.org/0000-0003-3347-6518*

Daniel Errandonea – *Departamento de Física Aplicada - Instituto de Ciencia de Materiales, MALTA Consolider Team, Universidad de Valencia, Edificio de Investigación, 46100 Valencia, Spain; orcid.org/0000-0003-0189-4221*

Complete contact information is available at:

<https://pubs.acs.org/10.1021/acs.inorgchem.1c03878>

Notes

All relevant data are available from the corresponding author upon reasonable request.

The authors declare no competing financial interest.

ACKNOWLEDGMENTS

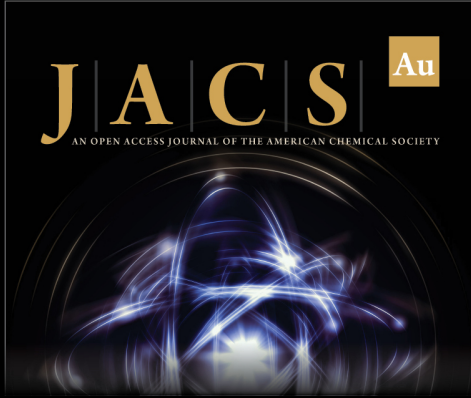
The authors acknowledge financial support from the Spanish Research Agency (AEI) and Spanish Ministry of Science and Investigation (MCIN) under projects PID2019106383GB-C41/C43/C44 (DOI: 10.13039/501100011033), and projects PGC2018-101464-B-I00 and PGC2018-097520-A-I00 (cofinanced by EU FEDER funds). The authors acknowledge financial support from the MALTA Consolider Team network, under project RED2018-102612-T. R.T. acknowledges funding from the Spanish Ministry of economy and competitiveness (MINECO) via the Juan de la Cierva Formación program (FJC2018-036185-I). J.G.P. thanks the Servicios Generales de Apoyo a la Investigación (SEGAI) at the University of La Laguna. A.L. and D.E. would like to thank the Generalitat Valenciana for the Ph.D. fellowship GRISOLIAP/2019/025, and the authors would also like to thank them for funding under the Grant Prometeo/2018/123 (EFIMAT). The authors also thank ALBA synchrotron light source for funded experiment under proposal numbers 2020074389 and 2020074398 at the MSPD-BL04 beamline.

REFERENCES

- (1) Hassan, A.; Iqbal, T.; Tahir, M. B.; Afsheen, S. A review on copper vanadate-based nanostructures for photocatalysis energy production. *Int. J. Energy Res.* **2019**, *43*, 9–28.
- (2) Guo, W.; Chemelewski, W. D.; Mabayoje, O.; Xiao, P.; Zhang, Y.; Mullins, C. B. Synthesis and characterization of CuV_2O_6 and $\text{Cu}_2\text{V}_2\text{O}_7$: Two photoanode candidates for photoelectrochemical water oxidation. *J. Phys. Chem. C* **2015**, *119*, 27220–27227.
- (3) Song, A.; Chemseddine, A.; Ahmet, I. Y.; Bogdanoff, P.; Friedrich, D.; Abdi, F. F.; Berglund, S. P.; van de Krol, R. Evaluation of copper vanadate ($\beta\text{-Cu}_2\text{V}_2\text{O}_7$) as a photoanode material for photoelectrochemical water oxidation. *Chem. Mater.* **2020**, *32*, 2408–2419.
- (4) Mercurio-Lavaud, D.; Frit, B. Structure cristalline de la variété basse température du pyrovanadate de cuivre: $\text{Cu}_2\text{V}_2\text{O}_7\text{-}\alpha$. *Acta Crystallogr. B* **1973**, *29*, 2737–2741.
- (5) Calvo, C.; Faggiani, R. α Cupric divanadate. *Acta Crystallogr. B* **1975**, *31*, 603–605.
- (6) Hughes, J. M.; Birnie, R. W. Ziesite, $\beta\text{-Cu}_2\text{V}_2\text{O}_7$, a new copper vanadate and fumarole temperature indicator. *Am. Mineral.* **1980**, *65*, 1146–1149.
- (7) Clark, G. M.; Garlick, R. Formation and properties of copper (II) divanadate (V). *J. Inorg. Nucl. Chem.* **1978**, *40*, 1347–1349.
- (8) Rao, N. S.; Palanna, O. G. Phase transition in copper (II) pyrovanadate. *Bull. Mater. Sci.* **1993**, *16*, 37–43.
- (9) Krivovichev, S. V.; Filatov, S. K.; Cherepansky, P. N.; Armbruster, T.; Pankratova, O. Y. Crystal structure of $\gamma\text{-Cu}_2\text{V}_2\text{O}_7$ and its comparison to blossite ($\alpha\text{-Cu}_2\text{V}_2\text{O}_7$) and ziesite ($\beta\text{-Cu}_2\text{V}_2\text{O}_7$). *Canad. Mineral.* **2005**, *43*, 671–677.
- (10) Yashima, M.; Suzuki, R. O. Electronic structure and magnetic properties of monoclinic $\beta\text{-Cu}_2\text{V}_2\text{O}_7$: A GGA+U study. *Phys. Rev. B* **2009**, *79*, 125201.
- (11) He, Z.; Ueda, Y. Paramagnetic anisotropy and spin-flop transition in single crystals of the quasi-one-dimensional system $\beta\text{-Cu}_2\text{V}_2\text{O}_7$. *Phys. Rev. B* **2008**, *77*, 052402.
- (12) Banerjee, A.; Sannigrahi, J.; Bhowal, S.; Dasgupta, I.; Majumdar, S.; Walker, H. C.; Bhattacharyya, A.; Adroja, D. T. Spin wave excitations in the pyrovanadate $\alpha\text{-Cu}_2\text{V}_2\text{O}_7$. *Phys. Rev. B* **2016**, *94*, 144426.
- (13) Tsirlin, A. A.; Janson, O.; Rosner, H. $\beta\text{-Cu}_2\text{V}_2\text{O}_7$: A spin-1/2 honeycomb lattice system. *Phys. Rev. B* **2010**, *82*, 144416.
- (14) Zhang, N.; Li, L.; Wu, M.; Li, Y.; Feng, D.; Liu, C.; Mao, Y.; Guo, J.; Chao, M.; Liang, E. Negative thermal expansion and electrical properties of $\alpha\text{-Cu}_2\text{V}_2\text{O}_7$. *J. Eur. Ceram. Soc.* **2016**, *36*, 2761–2766.
- (15) Wang, H.; Yang, M.; Chao, M.; Guo, J.; Gao, Q.; Jiao, Y.; Tang, X.; Liang, E. Negative thermal expansion property of $\beta\text{-Cu}_2\text{V}_2\text{O}_7$. *Solid State Ion.* **2019**, *343*, 115086.
- (16) He, Z.; Ueda, Y. Flux growth of $\beta\text{-Cu}_2\text{V}_2\text{O}_7$ single crystals in a closed crucible. *Cryst. Growth Des.* **2008**, *8*, 2223–2226.
- (17) Sato, M.; Warne-Lang, V.; Kadowaki, Y.; Katayama, N.; Okamoto, Y.; Takenaka, K. Sol–gel synthesis of doped $\text{Cu}_2\text{V}_2\text{O}_7$ fine particles showing giant negative thermal expansion. *AIP Adv.* **2020**, *10*, 075207.
- (18) Fauth, F.; Peral, I.; Popescu, C.; Knapp, M. The new material science powder diffraction beamline at ALBA synchrotron. *Powder Diffr.* **2013**, *28*, S360–S370.
- (19) *CrysAlis PRO*; Agilent Technologies: Yarnton, England, 2010.
- (20) *Rigaku Oxford Diffraction - CrysAlisPro Software system*, version 1.171.41.99a; Rigaku Corporation: Oxford, U.K., 2021.
- (21) Angel, R.; Gonzalez-Platas, J. Absorb-7 and Adsorb-GUI for single-crystal absorption corrections. *J. Appl. Crystallogr.* **2013**, *46*, 252–254.
- (22) Klotz, S.; Chervin, J. C.; Munsch, P.; Le Marchand, G. Hydrostatic limits of 11 pressure transmitting media. *J. Phys. D* **2009**, *42*, 075413.
- (23) Shen, G.; Wang, Y.; Dewaele, A.; Wu, C.; Fratanduono, D. E.; Eggert, J.; Klotz, S.; Dziubek, K. F.; Loubeyre, P.; Fat'yanov, O. V.; et al. Toward an international practical pressure scale: A proposal for an IPPS ruby gauge (IPPS-Ruby2020). *High Press. Res.* **2020**, *40*, 299–314.
- (24) Sheldrick, G. M. Crystal structure refinement with SHELXL. *Acta Crystallogr. C: Struct. Chem.* **2015**, *71*, 3–8.
- (25) Gonzalez-Platas, J.; Alvaro, M.; Nestola, F.; Angel, R. EosFit7-GUI: a new graphical user interface for equation of state calculations, analyses and teaching. *J. Appl. Crystallogr.* **2016**, *49*, 1377.
- (26) Birch, F. Finite Elastic Strain of Cubic Crystals. *Phys. Rev.* **1947**, *71*, 809–824.
- (27) Angel, R. J. Equations of state. *Rev. Mineral. Geochem.* **2000**, *41*, 35.
- (28) Hohenberg, P.; Kohn, W. Inhomogeneous electron gas. *Phys. Rev. B* **1964**, *136*, B864.
- (29) Kresse, G.; Furthmüller, J. Efficiency of *ab-initio* total energy calculations for metals and semiconductors using a plane-wave basis set. *Comput. Mater. Sci.* **1996**, *6*, 15–50.
- (30) Kresse, G.; Furthmüller, J. Efficient iterative schemes for *ab initio* total-energy calculations using a plane-wave basis set. *Phys. Rev. B* **1996**, *54*, 11169.
- (31) Blöchl, P. E. Projector augmented-wave method. *Phys. Rev. B* **1994**, *50*, 17953–17979.
- (32) Kresse, G.; Joubert, D. From ultrasoft pseudopotentials to the projector augmented-wave method. *Phys. Rev. B* **1999**, *59*, 1758.
- (33) Armiento, R.; Mattsson, A. E. Functional designed to include surface effects in selfconsistent density functional theory. *Phys. Rev. B* **2005**, *72*, 085108.
- (34) Mattsson, A. E.; Armiento, R.; Paier, J.; Kresse, G.; Wills, J. M.; Mattsson, T. R. The AM05 density functional applied to solids. *J. Chem. Phys.* **2008**, *128*, 084714.
- (35) Dudarev, S. L.; Botton, G. A.; Savrasov, S. Y.; Humphreys, C. J.; Sutton, A. P. Electron-energy-loss spectra and the structural stability of nickel oxide: An LSDA+U study. *Phys. Rev. B* **1998**, *57*, 1505.
- (36) Anisimov, V. I.; Zaanen, J.; Andersen, O. K. Band theory and Mott insulators: Hubbard U instead of Stoner I. *Phys. Rev. B* **1991**, *44*, 943.
- (37) Bhowal, S.; Sannigrahi, J.; Majumdar, S.; Dasgupta, I. A comparative study of electronic, structural, and magnetic properties of $\alpha\text{-}$, $\beta\text{-}$, and $\gamma\text{-Cu}_2\text{V}_2\text{O}_7$. *Phys. Rev. B* **2017**, *95*, 075110.


- (38) Hinuma, Y.; Pizzi, G.; Kumagai, Y.; Oba, F.; Tanaka, I. Band structure diagram paths based on crystallography. *Comput. Mater. Sci.* **2017**, *128*, 140–184.
- (39) Ganose, A. M.; Jackson, A. J.; Scanlon, D. O. sumo: Command-line tools for plotting and analysis of periodic *ab initio* calculations. *J. Open Source Softw.* **2018**, *3*, 717.
- (40) Momma, K.; Izumi, F. VESTA: a three-dimensional visualization system for electronic and structural analysis. *J. Appl. Crystallogr.* **2008**, *41*, 653–658.
- (41) Vali, A.; Sarker, H. P.; Heredia Cervera, B.; Rodríguez-Gutiérrez, I.; Hossain, M. K.; Huda, M. N.; Oskam, G.; Rajeshwar, K. Optical, Electrochemical, and Photoelectrochemical Behavior of Copper Pyrovanadate: A Unified Theoretical and Experimental Study. *J. Phys. Chem.* **2021**, *125*, 19609–19620.
- (42) Schönherr, T.; Atanasov, M.; Adamsky, H. Angular overlap model. *Comprehensive Coordination Chemistry II* **2003**, *2*, 443–455.
- (43) Sugano, S. *Multiplets of Transition-Metal Ions in Crystals*; Elsevier, 2012.
- (44) Ruiz-Fuertes, J.; Segura, A.; Rodríguez, F.; Errandonea, D.; Sanz-Ortiz, M. N. Anomalous high-pressure Jahn-Teller behavior in CuWO_4 . *Phys. Rev. Lett.* **2012**, *108*, 166402.
- (45) Burns, R. G. *Mineralogical Applications of Crystal Field Theory*; Cambridge University Press, 1993.
- (46) Lever, A. P. Inorganic electronic spectroscopy. In *Studies in Physical and Theoretical Chemistry*; Elsevier, 1984.
- (47) Drickamer, H. G.; Frank, C. W. *Electronic Transitions and the High Pressure Chemistry and Physics of Solids*; Springer Science & Business Media, 2013.
- (48) Li, J.; Struzhkin, V. V.; Mao, H. K.; Shu, J.; Hemley, R. J.; Fei, Y.; Mysen, B.; Dera, P.; Prakapenka, V.; Shen, G. Electronic spin state of iron in lower mantle perovskite. *Proc. Natl. Acad. Sci. U. S. A.* **2004**, *101*, 14027–14030.
- (49) Duclos, S. J.; Vohra, Y. K.; Ruoff, A. L. Pressure dependence of the 4T_2 and 4T_1 absorption bands of ruby to 35 GPa. *Phys. Rev. B* **1990**, *41*, 5372.
- (50) Gómez-Salces, S.; Aguado, F.; Rodríguez, F.; Valiente, R.; González, J.; Haumont, R.; Kreisel, J. Effect of pressure on the band gap and the local FeO_6 environment in BiFeO_3 . *Phys. Rev. B* **2012**, *85*, 144109.
- (51) Barreda-Argüeso, J. A.; Aguado, F.; Gonzalez, J.; Valiente, R.; Nataf, L.; Sanz-Ortiz, M. N.; Rodríguez, F. Crystal-Field Theory Validity Through Local (and Bulk) Compressibilities in CoF_2 and KCoF_3 . *J. Phys. Chem. C* **2016**, *120*, 18788–18793.
- (52) Rodríguez, F.; Hernández, D.; Garcia-Jaca, J.; Ehrenberg, H.; Weitzel, H. Optical study of the piezochromic transition in CuMoO_4 by pressure spectroscopy. *Phys. Rev. B* **2000**, *61*, 16497.
- (53) Yamamoto, T.; Shinagawa, K.; Saito, T.; Tsushima, T. A calculation of electronic states in $\text{YBa}_2\text{Cu}_3\text{O}_x$. *Jpn. J. Appl. Phys.* **1992**, *31*, L327–L330.
- (54) Diaz-Anichtchenko, D.; Turnbull, R.; Bandiello, E.; Anzellini, S.; Achary, S. N.; Errandonea, D. Pressure-induced chemical decomposition of copper orthovanadate ($\alpha\text{-Cu}_3\text{V}_2\text{O}_8$). *J. Mater. Chem. C* **2021**, *9*, 13402–13409.
- (55) Diaz-Anichtchenko, D.; Santamaria-Perez, D.; Marqueño, T.; Pellicer-Porres, J.; Ruiz-Fuertes, J.; Ribes, R.; Ibañez, J.; Achary, S. N.; Popescu, C.; Errandonea, D. Comparative study of the high-pressure behavior of ZnV_2O_6 , $\text{Zn}_2\text{V}_2\text{O}_7$, and $\text{Zn}_3\text{V}_2\text{O}_8$. *J. Alloys Compd.* **2020**, *837*, 155505.
- (56) Cliffe, M. J.; Goodwin, A. L. PASCAL: a principal axis strain calculator for thermal expansion and compressibility determination. *J. Appl. Crystallogr.* **2012**, *45*, 1321–1329.
- (57) Knight, K. S. Analytical expressions to determine the isothermal compressibility tensor and the isobaric thermal expansion tensor for monoclinic crystals: application to determine the direction of maximum compressibility in jadeite. *Phys. Chem. Miner.* **2010**, *37*, 529–533.
- (58) Liang, A.; Rahman, S.; Saqib, H.; Rodriguez-Hernandez, P.; Munoz, A.; Nénert, G.; Yousef, I.; Popescu, C.; Errandonea, D. First-


Order Isostructural Phase Transition Induced by High Pressure in $\text{Fe}(\text{IO}_3)_3$. *J. Phys. Chem. C* **2020**, *124*, 8669–8679.



JACS Au
AN OPEN ACCESS JOURNAL OF THE AMERICAN CHEMICAL SOCIETY

Editor-in-Chief
Prof. Christopher W. Jones
Georgia Institute of Technology, USA

Open for Submissions 

pubs.acs.org/jacsau  ACS Publications
Most Trusted. Most Cited. Most Read.